Analysis of Asymmetrical Creep of a Ceramic at 1350°C by Digital Image Correlation

Paul Leplay, Olivier Lafforgue, François Hild

▶ To cite this version:

Paul Leplay, Olivier Lafforgue, François Hild. Analysis of Asymmetrical Creep of a Ceramic at 1350°C by Digital Image Correlation. Journal of the American Ceramic Society, 2015, 98 (7), pp.2240-2247. 10.1111/jace.13601 . hal-01218666

HAL Id: hal-01218666
https://hal.science/hal-01218666v1

Submitted on 21 Oct 2015

Journal of American Ceramic Society 2015

Analysis of asymmetrical creep of a ceramic at 1350°C by Digital Image Correlation

Paul Leplay[1], *Saint-Gobain, Centre de Recherches et d'Etudes Européen, 550 avenue Alphonse Jauffret, CS 20224, F-84306 Cavaillon, France.*
Olivier Lafforgue, *Saint-Gobain, Centre de Recherches et d'Etudes Européen, 550 avenue Alphonse Jauffret, CS 20224, F-84306 Cavaillon, France.*
François Hild, *LMT-Cachan, ENS Cachan / CNRS / Université Paris Saclay, 61 Avenue du Président Wilson, F-94235 Cachan, France.*

Abstract

The glass industry requires the use of innovative ceramics that enable for long lifetimes. At very high temperatures, one of the key parameters for ceramics is their creep resistance. The characterization of the creep behavior, usually assessed through flexural tests, can be complex when an asymmetry appears between tension and compression. To detect and quantify such asymmetrical behaviors, the use of Digital Image Correlation (DIC) is proposed. First, several challenges are to be tackled for DIC at high temperature, namely, the random pattern stability, the radiation filtering and the heat haze. They are exacerbated by the limited possibilities to heat ceramics, the nonuniform strain fields and their low levels. Beyond several experimental developments, the strain uncertainties are decreased thanks to the use of two global approaches of DIC based on *ad hoc* finite-element kinematics. Last, the proposed methodology is applied to the analysis of asymmetric creep at 1350°C of an industrial zircon ceramic designed for its high creep resistance.

1. Introduction

In the glass industry, the ceramics used in furnaces or for forming are subjected to extreme conditions in terms of temperature, corrosion and creep. The development of innovative ceramics with optimal chemical and mechanical properties is a scientific and industrial challenge for the suppliers. Among the previously listed properties, creep is one of the most prevalent design parameters to ensure the lifetime of ceramic structures at high temperatures.[1, 2, 3] For a reliable analysis of the final creep resistance, a rigorous approach consists of first performing mechanical creep tests at high temperatures, then identifying the parameters of a suitable constitutive law and finally running numerical simulations to predict the lifetime in various applications.

The first step is devoted to creep tests. For ceramic materials, 3-point or 4-point flexure is one of the most common mechanical tests thanks to its easy implementation.[4] However, its main drawback is the nonuniform strain/stress field, which implies to be able to distinguish tensile from compressive responses. Most of the time, the tensile and compressive behaviors are assumed to be symmetric so that the vertical deflection measurement is sufficient to calculate the flexural creep strain assuming perfect boundary conditions. But many ceramics, especially at high temperatures, may have an asymmetric creep behavior.[5, 6, 7] For such ceramics, uniaxial tensile tests may be performed, yet they are very delicate.[8] Compression and flexural tests have been considered,[9] even though the identification of the tensile behavior is not straightforward. A final route is to only perform flexural tests, but with a more complex strain measurement technique. For instance, several

---

[1] Corresponding email address: paul.leplay@saint-gobain.com

strain gauges can be used,[10] although the real boundary conditions of the test remain partially assessed. An alternative consists of resorting to full-field measurements not only to assess the actual boundary conditions, but also to measure the strain field of the sample. Since high temperatures are reached, non-contact techniques are desirable. Among them,[11] Digital Image Correlation (DIC) has been chosen for its high potential for direct link with numerical simulations.

DIC has already been applied to analyze high temperature experiments. Lyons et al.[12] have shown its feasibility up to 650°C when samples were subjected to translations, thermal expansion and tensile loads. Then creep crack growth was studied in the vicinity of the crack tip for experiments on a nickel-based super-alloy up to 700°C[13]. Pan et al.[14] showed that ordinary equipment can be used to evaluate coefficients of thermal expansion of various metallic materials. Leplay et al.[7] studied the damage behavior of aluminum titanate by performing four-point flexural tests up to 900°C. The feasibility of reliable DIC measurements up to 1200°C has been shown by Grant et al.[15], Pan et al.[16] and Hammer et al.[17]. Last, Novak and Zok[18] achieved temperatures up to 1500°C by controlling the illumination and filtering, and minimizing heat haze effects. Moreover they proposed speckling procedures that allowed for reliable DIC analyses. It is worth noting that stereo DIC is seldom used in these high temperature analyses[18]. De Strycker et al.[19] evaluated the coefficient of thermal expansion of stainless steels during a cooling from 600°C outside the furnace.

Among all the previous cited works, three main challenges for DIC at high temperature are systematically listed:

- The first issue is related to the surface random texture required for DIC. Up to 300°C, it was shown that regular paint was sufficient.[20] So-called high temperature paints can be used up to 600°C. However, this solution becomes not always feasible at higher temperatures.[17, 19] For instance, boron nitride combined with aluminum oxide was used by Lyons et al.[12]. Pan et al.[16] propose to mix cobalt oxide with commercial inorganic adhesive to reach temperatures up to 1200°C.
- As pointed out early on by Lyons et al.[12], special care should be exercised at high temperature since the so-called black body radiations will lead to violations of brightness conservation. One remedy is to use more powerful lighting devices. However, there is a limit when temperatures of the order of 800°C are reached. Another solution is to use band pass filters to reach higher temperatures.[14, 15, 16] It is also possible to work with ultra-violet light to avoid any radiation.[21]
- The last issue is related to the existence of a temperature gradient between the sample and the camera lens that induces a variation of the refractive index of the air. Even a constant temperature gradient generates an additional artifact for the optical path. However the main issue is related to varying thermal gradients in the air due to convection at high temperatures. One solution is to use an air flux to homogenize the heat haze effects.[12, 17, 18] Other authors simply neglect these phenomena.[14, 16] The heat haze influence is very dependent on the experimental setup and the way the sample is heated. The worst case is to have a traditional furnace since a large amount of air is then subjected to heat haze between the sample, the window and the lens of the camera.[7, 12, 17] An alternative route is to resort to induction,[15] laser[18] or infrared[14, 16] heating. These solutions limit the convection effects related to the air flow but cannot be applied to every class of materials, in particular to ceramics.

To have a better overview of the existing state of art and thus a good understanding of the objectives of the present paper, the main applications of DIC at high temperature are summarized and compared in *Table 1*. Several remarks can be made. First, most of the studies deal with metallic materials. It means that the heat haze can be minimized by the several types of possible heating devices and the final strain level is greater than 1-2 %. Second, the main goal is often to measure mean strains over a large region of interest so that the accuracy of the measured final value is improved. Third, the final strain uncertainties are seldom explicitly estimated.

Year / Reference	**Temperature (°C)**	**Objective**	**Material**	**Heating**	**Max. strain**	**Std. strain resolution**	**Pattern**
1996 [12]	[25-650]	Mean CTE/tensile strains	Superalloys	Furnace	0.8%	0.02% at 650°C	Boron nitride / Aluminum oxide
2009 [15]	[25-1000]	Mean CTE/tensile strain	Superalloy	Ohmic	2%	NA	abraded surface
2011 [16]	[25-1200]	Mean CTE strain	Stainless steel	Radiation	2%	NA	Cobalt oxide / inorganic adhesive
2011 [18]	[25-1500]	Mean CTE and strain field	Superalloy / C/SiC composite	Laser	2%	0.04% at 800°C	Alumina/Zirconia
2012 [7]	[600-900]	Strains in flexure	Ceramic	Furnace	0.5%	0.05% at 900°C	NA
2013 [22]	[25-1550]	Mean CTE and strain field	Stainless steel C/SiC composite	Radiation	4%	0.5% at 1300°C	Pre-oxidized / ceramic coating
2014 [21]	[100-1150]	Mean strain in tension / CTE	Superalloy	Induction	2%	0.5% at 725°C	Pre-oxidized / VHT paint
2014 [17]	600	Mean strain in tension	Ti-6Al-4V	Furnace	25%	NA	Rustoleum paint
2014 [23]	2600	Mean strain in tension	Carbon	Ohmic	4%	NA	Sprayed tungsten
2014 [24]	720	Necking in tension	Steel	Induction	30%	NA	Electrochemical

Table 1 – Overview of the existing works on DIC at high temperature

The goal of this paper is to address asymmetrical creep in a flexural test at 1350°C. Compared with existing works (*Table 1*), it requires a stable paint pattern for ceramics at this temperature, a control of the important heat haze generated by the use of a traditional furnace, the measurement of non-uniform strain fields and very low uncertainties, down to at least 0.01 % given the low strain levels of ceramics. To reach these objectives, the paper is organized as follows. In Section 2, the two DIC methods used herein are presented. Section 3 deals with the experimental set-up, the sample preparation, the correction of the radiation and heat haze effects. A thorough uncertainty analysis is then performed. The results are given in Section 4 for an industrial zircon ceramic in terms of its asymmetrical creep behavior at 1350°C.

2. Digital Image Correlation methods

2.1 Local DIC

In the sequel, DIC will be used to measure strain fields at elevated temperatures. In all the above-cited works, except Ref.[7], local approaches to DIC were considered. In the present case, an alternative route will be followed since small strain levels are sought in conjunction with a good spatial resolution, namely, global approaches to DIC. [25]

2.2 Global DIC

Global approaches to DIC consist of performing the registration over the whole Region Of Interest (ROI). One advantage lies in the fact that the continuity of the displacement field is automatically satisfied. Let us consider the gray level picture f in the reference configuration, and g the picture in the deformed configuration. The conservation of gray level reads

$$f(\mathbf{x}) = g(\mathbf{x} + \mathbf{u}(\mathbf{x})) \tag{1}$$

where $\mathbf{x}$ is any pixel within the ROI. To measure the displacement field $\mathbf{u}(\mathbf{x})$, a weak form of the previous equation is considered, namely, the sum of squared differences

$$\Phi_c = \sum_{ROI} \left(f(\mathbf{x}) - g(\mathbf{x} + \mathbf{u}(\mathbf{x})) \right)^2 \tag{2}$$

is minimized with respect to the chosen kinematic parameterization of the experiment at hand. In the present study two different kinematic bases are considered. First (Section 2.2.1), a general purpose description corresponds to the choice of a finite-element based DIC approach.[27] Second (Section

2.2.2), as already proposed when flexural experiments are performed,[28, 29] a beam kinematics will also be implemented.

To validate the choice of any kinematic basis and thus the measured displacement field, the correlation residual ρ is defined as the gray level difference for any pixel of the region of interest in the reference configuration $f(\mathbf{x})$ and that of the picture in deformed configuration corrected by the measured displacement $g(\mathbf{x}+\mathbf{u}(\mathbf{x}))$

$$\rho(\mathbf{x}) = f(\mathbf{x}) - g(\mathbf{x}+\mathbf{u}(\mathbf{x})) \tag{3}$$

which should be as close as possible to the acquisition noise.

2.2.1 Finite-element kinematics: Q4-DIC

In the present experiment, it is expected that the displacement field is continuous. One of the simplest kinematic bases is associated with 4-noded quadrilaterals. In the element frame ($-1 \le x \le 1$, $-1 \le y \le 1$), the shape functions N_i (i = 1,4) read

$$N_i(x,y) = \frac{1}{4}(1 \pm x)(1 \pm y) \tag{4}$$

so that the two components of the elementary displacement field are expressed as

$$u_x^e(x,y) = \sum_{i=1,4} \xi_i N_i(x,y) \quad \text{and} \quad u_y^e(x,y) = \sum_{i=1,4} \upsilon_i N_i(x,y) \tag{5}$$

where ξ_i and υ_i are the nodal displacements, along two perpendicular directions of the considered element e.

2.2.2 Beam kinematics: Beam-DIC

Since a four-point flexural test is analyzed, a reduced kinematics is also devised. It is based on an Euler-Bernoulli hypothesis.[30] Five displacement fields are considered.[29] First, in the central part of the beam submitted to four-point flexure, only three kinematic degrees of freedom are needed, namely, the (constant) curvature κ, a rigid body rotation θ and vertical translation ϖ. In the horizontal direction, two degrees of freedom υ_0 and υ_1 are needed to describe a rigid body translation and tension/compression. The latter may be induced by the friction on the various supports of the flexural setup. The displacement of any point of dimensionless coordinates (x,y) reads

$$\begin{Bmatrix} u_x^b(x,y) \\ u_y^b(x,y) \end{Bmatrix} = \begin{bmatrix} -xy & -y & 0 & 1-x & x \\ \dfrac{x^2}{2} & x & 1 & 0 & 0 \end{bmatrix} \begin{Bmatrix} L^2\kappa \\ L\theta \\ \varpi \\ \upsilon_0 \\ \upsilon_1 \end{Bmatrix} \tag{6}$$

where L denotes the beam length. The advantage of this last choice is that the number of unknowns has been drastically reduced so that the measurement uncertainties are lower.[28] Furthermore, the evaluation of the rotation and curvature does not require any post-processing as they are directly related to the measured degrees of freedom and the differentiations of Equation (6).

3. Experimental setup

3.1 Description of the material and the test

For the experimental work, an isopressed zirconium silicate product (ZS-ISO) made by Saint-Gobain SEFPRO is considered. This material is manufactured by cold isopressing followed by pressureless sintering. The ZS-ISO samples have a density of about 4000 kg/m^3 and an open porosity of about 5 %. In service, this ceramic undergoes extreme conditions, namely, temperature, corrosion and creep.

To evaluate the creep properties of such materials, a parallelepipedic sample ($h \times w \times L$ = 15 × 10 × 150 mm^3) is tested in a 4-point flexural device (outer span, D_1 = 120 mm, inner span D_2 = 40 mm) with a dead load of 129 N. Assuming a linear elastic behavior, this load level generates a tensile/compressive stress of about ± 7 MPa. In front of the furnace equipped with a window, a digital single-lens reflex (DSLR) camera is chosen for its large sensor size, its high definition and low cost (Canon 700D, APS-C sensor, 18 RGB Mpixels). To obtain a small enough angle of view, a 300-mm macro telephoto lens is used with a 2 × focal extender (*Figure 1*). One image is shot every 15 minutes for 45 hours. The physical size of the gray level pixel is 16.2 µm.

Measuring the response in flexure of ZS-ISO is challenging since this ceramic is designed to have a high creep resistance even at these temperature levels. It is possible neither to speed up creep, nor to wait too long. The final creep strain of ZS-ISO remains very low (*i.e.*, about 0.5-1.0 %), which is an issue for DIC measurements at such high temperatures. The strain uncertainties should be at least one to two orders of magnitude lower than the expected final strain levels. Therefore, specific experimental features must be considered for DIC at 1350°C.

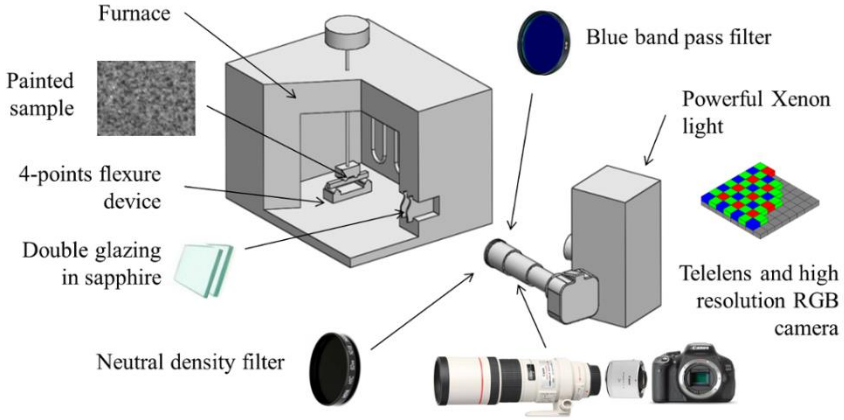

Figure 1 - Overview of the experimental set-up for creep tests and DIC at 1350°C

3.2 Specific experimental features for DIC at 1350°C

3.2.1 Paint pattern stability and surface contrast

Before the test begins, a random pattern must be deposited onto the sample surface for DIC purposes. The first challenge consists of finding a paint that is stable up to 1350°C for several days on this ceramic. An in-house solution was developed with a non-oxide powder (silicon carbide). The stability of this specific paint was checked for up to 200 hours at 1350°C on ZS-ISO samples. This pattern has a mean correlation radius of about 3 pixels, which is favorable for DIC analyses.[27, 31]

3.2.2 Blackbody radiations and image contrast

The painted sample is heated up to 1350°C. Above 800°C, the blackbody radiations become critical for the sensors of DSLR cameras, despite their inherent band pass filter to remove UV radiations (< 410 nm wavelengths) and IR radiations (> 710 nm wavelengths). At 1350°C, the intensity of the red channel is so high that the final image has no contrast at all, even with a 1000 W Xenon lamp used to lighten the sample. To be able to run DIC analyses at these temperature levels, the benefit of utilizing a blue filter has already been demonstrated.[15, 16, 21] Such a blue band pass filter prevents the blackbody radiations from being captured by the sensor. For a constant temperature test, the radiation level may not vanish provided it is constant. Consequently, a filter (*i.e.*, 470 ± 20 nm) is preferred since the green channels also record some information (*Figure 1*). It is worth remembering that the green sensors have the advantage of being twice as numerous as blue and red sensors in the

Bayer matrix in DSLR cameras. The blue and green channels are here both used, so that the final texture and dynamic range of gray level images is slightly enhanced. To still increase the final contrast, the image histogram is stretched directly when the 14-bit *.cr2 files are converted to 8-bit *.tif images.

3.2.3 Heat haze and image stability

The sample is heated inside a furnace with several electrical resistances. This type of heating enables for a homogenous thermal loading of ceramic materials (± 3°C variation in the present case inside the furnace). However, compared to other heating systems suited to metallic samples,[16,18,15 21] such a furnace generates a large amount of heat haze due to the varying refractive index of the hot air in front of the sample. This heat haze is problematic since DIC assumes that the differences from one image to another only come from a physical motion, and not from an optical artifact. A first solution consists of subtracting the heat haze influence to the DIC results, provided an accurate evaluation of all the dynamic motions of the air between the sample and the lens are quantified.[32] A second route is to minimize the heat haze as much as possible.[18] First, as proposed by Lyons et al.[12], a double glazing made of sapphire was used to close the furnace window to enable for the sample visualization without additional thermal heterogeneity and heat haze. Then, a fan was added to regularize the flow between the window and the lens. Although such a fan was supposed to minimize the heat haze,[12, 18] no significant benefit was observed in the present case. It would also be possible to add a fan directly inside the furnace to reduce the optical distortions due to temperature gradients.[17]

Once the heat haze is minimized as much as possible, it is possible to ‘average’ it. Instead of taking a lot of images during the test and averaging *a posteriori* the measured displacement fields,[19] it is proposed to average *a priori* the images and the heat haze influence as well. A neutral density opaque filter is used to strongly reduce the amount of light captured by the camera (*Figure 1*). Hence, the integration time of the camera is increased up to several seconds to take one single image with a correct exposure. The heat haze, which is assumed to be random, is continuously averaged over this period of time. Provided the exposure duration is long enough with respect to the heat haze frequency, the images are slightly blurred, but very stable. In that sense, to make an *a priori* average with 10-s image is equivalent to average *a posteriori* the results of one thousand 0.01s images. Fast creep rates in comparison with the time exposure may induce artifacts, but this is not the case in this work. The efficiency of such an approach with long exposure images is proven in the next part.

3.3 DIC strain uncertainties

To evaluate the optimal exposure duration, several configurations are tested at 1350°C. Seven series of 20 images are shot with an exposure duration ranging from 1/250 s to 30 s thanks to different neutral density filters. No load is applied so that no creep is expected, namely, no strains are expected. Therefore, the variations of the local strains for the 20 acquired images are considered as representative of all the artifacts and uncertainties associated with the experimental setup (e.g., DIC algorithm, sensor noise, heat haze). In the following analyses, the standard uncertainties are evaluated (*i.e.*, they correspond to the standard deviation of the reported quantity). The uncertainty analysis is carried out in two steps:

- First, a Gaussian white noise is added to each of the seven reference images. The added noise has a 3 gray level standard deviation, corresponding to the quality of the camera sensor at ISO100. The reference and noisy images are then registered with the two different DIC codes (*Figure 2*). The present standard strain uncertainties are about one order of magnitude higher than the usual uncertainties due to the subpixel interpolation. Again, the strain uncertainties only depend on the element size, but not on the exposure duration. Beam-DIC is much less sensitive to noise thanks to its low number of degrees of freedom in conjunction with the large size of its unique element. Last, both results are consistent since the extrapolated results of Q4-DIC tend to those of Beam-DIC. This *a priori* analysis shows that to reach very low standard strain uncertainties, Beam-DIC is desirable, provided the beam kinematics is consistent with the analyzed experiment.

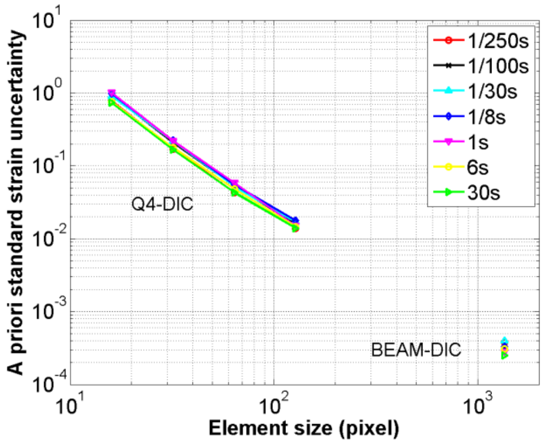

Figure 2 - A priori standard strain uncertainties due to numerical noise representative of the used camera

- Second, all the images of the seven series are correlated with respect to their own reference image (*Figure 3*). For the images shot at 1/250 s without neutral density filters, the standard strain uncertainties are very high (≈ 0.4 % for Q4-DIC with 64 × 64 pixel elements). The reason for such high levels is understood when analyzing the measured displacement field, which reveals the effect of heat haze (*Figure 4* left). Very coarse meshes help, but even with one large element and using Beam-DIC, the standard strain uncertainty is still of the order of 0.04 %. The standard strain uncertainties are reduced by one new order of magnitude when the exposure duration is greater than a few seconds. For 30-s images, the standard strain uncertainty is of the order of 0.05 % for Q4-DIC with 64 × 64 pixels, and 0.002 % with Beam-DIC with one element. This result means that the exposure duration is long enough with respect to the frequency of the heat haze. For Q4-DIC, a plateau is reached with the longest exposure durations. Others sources of uncertainties such as the previously studied numerical noise limit the accuracy of a local measurement (*Figure 4* right).

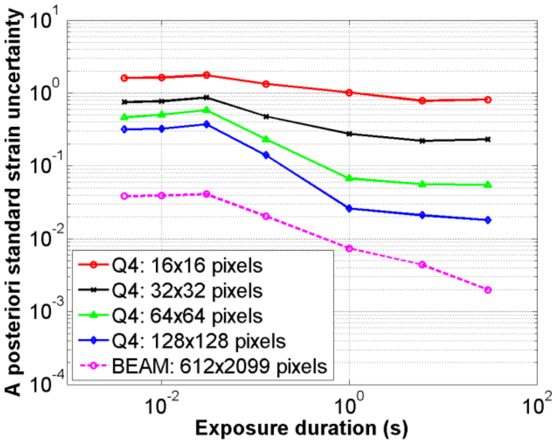

Figure 3 - A posteriori standard strain uncertainties mainly due to the heat haze and acquisition noise

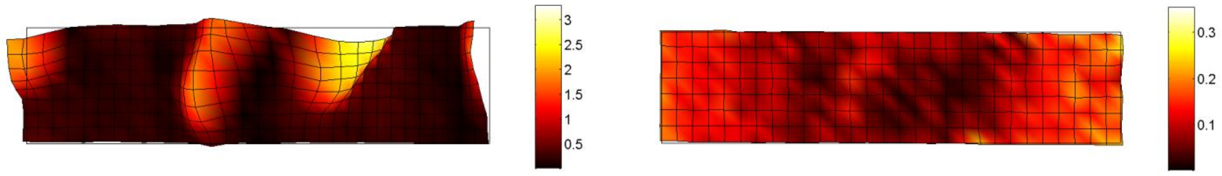

Figure 4 – Examples of deformed meshes (amplified by 50) obtained with Q4-DIC (64 × 64 pixel Q4 elements) for two images: 1/250 s (left) and 30 s (right) integration time. The absolute displacement field is expressed in pixel

The fact that the experimentally determined strain uncertainties (*Figure 5*) do not reach the *a priori* estimates (*Figure 4*) is an indication that the experimental configuration is very challenging for reliable DIC analyses. However, by increasing the time integration, the achieved uncertainties reach very low levels. The latter ones have been obtained by adapting the time integration and the spatial regularization provided by Q4- and Beam-DIC.

4. Asymmetrical creep behaviour of ZS-ISO at 1350°C

4.1 DIC general results with Q4-DIC and Beam-DIC

During the 45-hour creep test, 180 images with a 30-s exposure duration are shot. The reference image is acquired just after the weight is applied ($t = 0$ h). On the reference image, only the central zone between the two upper supports where the curvature is assumed to be constant is analyzed (*Figure 5*). This central zone is either divided into 504 elements of size 64 × 64 pixels for Q4-DIC, or used with one beam element of size 936 × 2345 pixels for Beam-DIC. For both approaches the measured displacement fields are corrected thanks to a small calibration sample put just below the tested sample. The former enables all rigid-body motions due to the furnace, the camera, and the tripod to be excluded from the displacement field measurements.

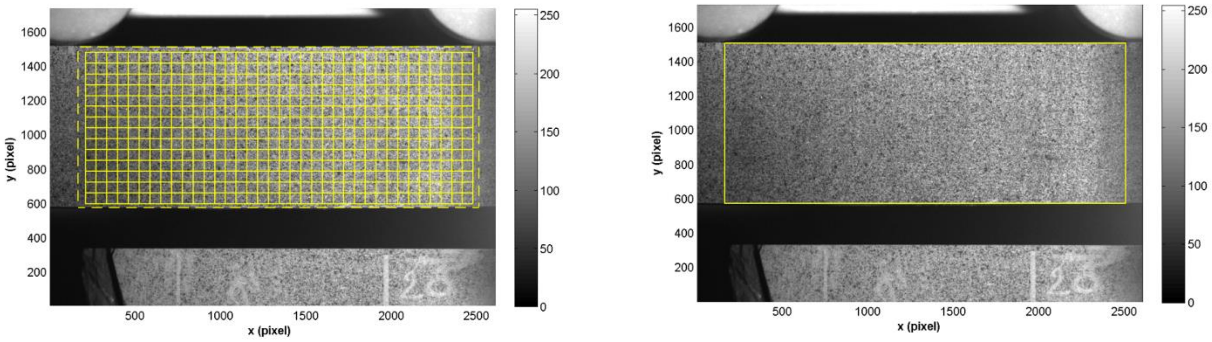

Figure 5 - Reference image at 1350°C, region of interest and mesh for Q4-DIC (left) and Beam-DIC (right).

First, the consistency of the measurement results is analyzed in terms of the final deformed shape (*Figure 6*). For Q4-DIC, which is obtained without any assumption on the flexural kinematics, the global shape of a bent sample is easily recognizable, no noise is visible and the horizontal displacement amplitude is consistent with the results of Beam-DIC (*i.e.*, –9.3 to 11.2 pixels or –150 to 181 µm).

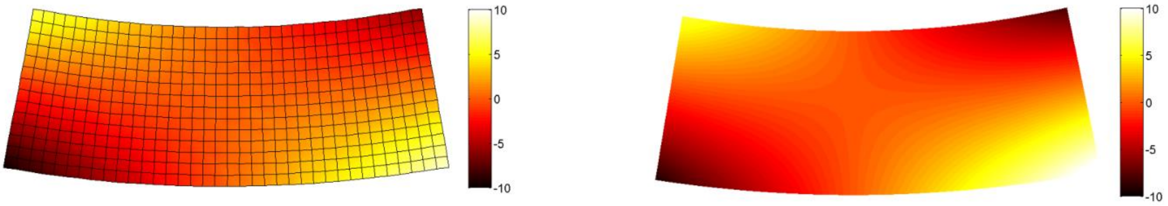

Figure 6 - Final deformed mesh (amplified by 10) for Q4-DIC (left) and Beam-DIC (right). The longitudinal displacement field is also shown and expressed in pixels

The consistency of the results is also checked with the correlation residuals. They are initially quite low (about 2% of the dynamic range) but end at a rather high level (6-9% of the dynamic range) after 45h. With respect to standard room temperature tests, these levels should be considered as problematic. However it is believed that this gradual increase reveals the slow degradation of the non-oxide powder pattern.

The vertical displacements are analyzed via the deflection profiles (*Figure 7*). The latter is calculated as the mean vertical displacement for each vertical section of the beam (*i.e.*, all vertical nodes for Q4-DIC, all vertical pixels for Beam-DIC). As expected from *Figure 8*, the final deflection profile corresponds to a 2nd order polynomial. The final maximum vertical deflection is equal to 1493 µm (or 92.2 pixels) near the center of the sample. This deflection level corresponds to what would have been recorded by a displacement sensor as classically used in flexural tests without DIC. On these deflection profiles, a slight unbalance between the left and right sides is noticed. It means that this 4-point flexural test is not perfectly balanced, namely, the total weight was probably not correctly put in the middle of the two upper supports. Moreover, the two DIC results are fully consistent.

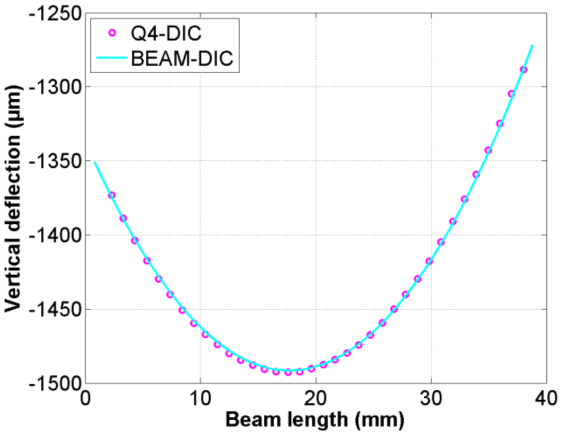

Figure 7 - Final vertical deflection profiles for Q4-DIC and Beam-DIC

From the strain fields shown in next part, it is possible to calculate that the strain levels are on average 10% higher on the left part of the sample. It confirms that this four-point flexural test was not fully balanced between the left and right. For a better analysis of the test imperfection, it is worth noting that it would be possible to use an identification approach based on DIC results taking into account these effects.[33]

4.2 Quantification of the asymmetrical creep behavior

The longitudinal strain fields better reveal the differences between the two DIC approaches (*Figure 8*). In Beam-DIC (right), the horizontal field varies linearly with the vertical coordinate since it is directly computed from analytical functions (*Equation (6)*). The minimum and maximum final strains are directly available, namely, $\varepsilon_{comp} = -0.619\ \%$ and $\varepsilon_{tens} = +0.877\ \%$ after 45h. It corresponds to a ratio of about 1.42 between the tensile and compressive strains. For Q4-DIC, the strain amplitude ranges from – 0.76 % at the bottom and + 1.10 % at the top of the beam. A tension/compression asymmetry is also detected, but with a lower accuracy. The strains obtained with Q4-DIC have an uncertainty of the order of 0.09 %, which is consistent with the uncertainty analysis performed previously (*Section 3.3*).

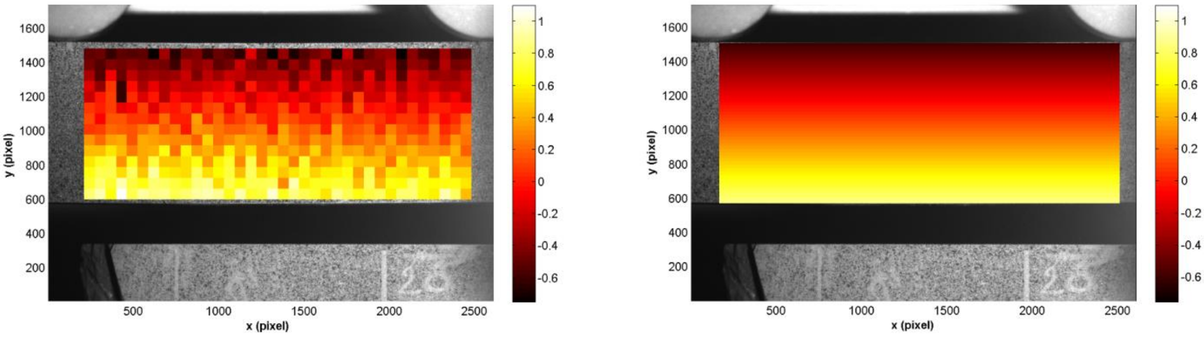

Figure 8 - Horizontal strain fields (expressed in %) as obtained with Q4-DIC (left) and Beam-DIC (right)

With Q4-DIC, to obtain reliable strain values in tension and compression, *a posteriori* assumptions have to be added (*Figure 9*). Thanks to the constant curvature in the central zone of four-point flexure, the local strains are horizontally averaged. These mean values are then linearly interpolated and extrapolated to reach the sample edges. This post-processing yields a compressive strain of $\varepsilon_{comp} = -0.620\ \%$ and a tensile strain of $\varepsilon_{tens} = +0.883\ \%$, which is very close to the results obtained directly via Beam-DIC.

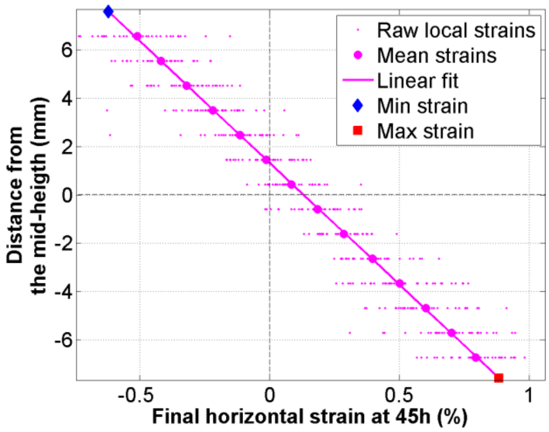

Figure 9 - Post-processing Q4-DIC results to estimate the horizontal strain profile

The change of the tensile and compressive strains is plotted in *Figure 10*. These strains are compared to an analytical value calculated from the vertical deflection measurement (*i.e.*, a ‘virtual’ displacement sensor). The maximum deflection is either corrected by the motions of the reference sample (*Figure 7*), or not. Several remarks are drawn:

- Since DIC is started after the initial load has been applied, the measured strain field corresponds to the current total strain minus the initial elastic strain.[6]
- The strain values obtained by Q4-DIC and Beam-DIC are equal within ± 0.01 % margin. In the present case, adding the flexural assumption *a posteriori* or *a priori* does not make a big difference.
- No significant primary creep is observed for this ZS-ISO ceramic, namely, the creep rate is constant only a few hours after the test begins.
- The mean linear creep rate is 2×10^{-4} / h in tension, and 1.35×10^{-4} /h in compression; it corresponds to a tension/compression ratio about 1.5. The first 10 hours are excluded from this analysis in case primary creep occurred.
- When the raw deflection is not corrected with respect to the reference sample, the resulting strain lies between the tensile and compressive DIC strains, but its value is noisy.
- When the raw deflection is corrected by removing the spurious motions, the strain value is much more regular and is now equal to the average between the tensile and compressive strains (*i.e.*, the classical link between deflection and strains in flexure with a symmetric response).

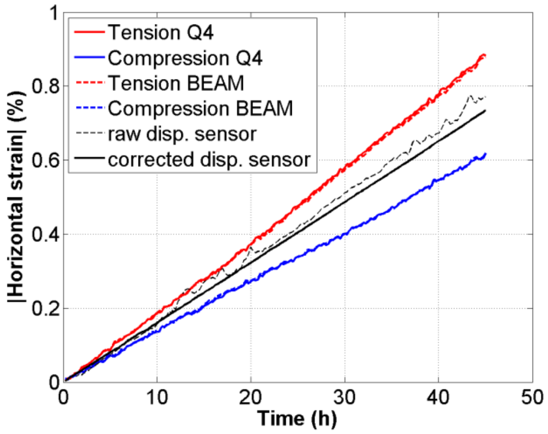

Figure 10 - History of the tensile and compressive creep strains

It is worth noting that the uncertainties for the tensile and compressive strains are extremely low. The distribution of the difference between the strain profiles and linear creep rates is Gaussian and its standard variation is as low as 0.007%. Adding *a priori* or *a posteriori* hypotheses on the flexural kinematics enables the strain uncertainty level to be reduced by one order of magnitude with respect to the local values of Q4-DIC (*Figure 8*). To the authors' knowledge, this uncertainty level has not been reached at such high temperature, in particular above 1000°C.

Last, with these extreme strain values in flexure, ε_{tens} and ε_{comp}, it is possible to calculate the location of the neutral axis. With respect to the sample mid-height, the distance h_n is defined as the axis where the creep strain vanishes

$$h_n = \left(\frac{\varepsilon_{tens}+\varepsilon_{comp}}{\varepsilon_{tens}-\varepsilon_{comp}}\right)\frac{h}{2} \qquad (7)$$

The neutral axis location is erratic at the beginning of the test when the strain levels are very low (*Figure 11*). As the strain levels increase, the neutral axis location is more and more accurately determined, and its final location is estimated to 1.3 ± 0.1 mm for the two DIC approaches. Since the approach with the deflection measurement assumes intrinsically a symmetric behavior, the neutral axis does not move from the mid-height.

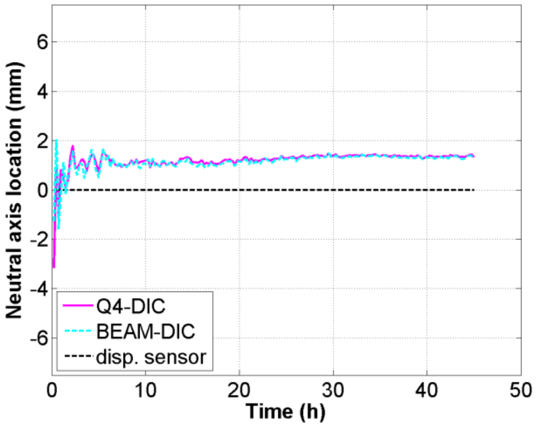

Figure 11 - Location of the neutral axis, h_n, during the creep test

The two approaches developed herein, namely, Q4-DIC and Beam-DIC, have yielded consistent quantifications of the asymmetrical creep behavior of the studied ZS-ISO ceramic at 1350°C in terms of vertical deflection measurements, minimum and maximum flexural strains, creep rates and neutral axis location.

5. Conclusion

To develop some innovative ceramics for glass industry, the issue of reliable creep characterization must be tackled, especially in case of asymmetry between tension and compression. DIC has been used herein to monitor a creep flexural test at 1350°C on an industrial zircon ceramic.

To be able to measure very low strains by DIC at such high temperatures, several experimental challenges have been addressed, especially the effects of heat haze that have been continuously averaged thanks to neutral density filters. Compared with the initial configuration, one order of magnitude on the standard strain uncertainties has been gained thanks to long exposure images. To decrease the strain uncertainties by a second order of magnitude, two global DIC approaches based on the known specific kinematics in flexure are used to measure the tensile and compressive strains. Standard strain uncertainties of the order of 0.007 % have been achieved during the entire creep test. Under these conditions, it has been shown that the creep strain rate is about 1.5 times higher in tension than in compression. Such an asymmetry would have been impossible to detect with the classical measurement devices of the vertical deflection.

Some test imperfections, such as left/right unbalance in four-point flexure, have been observed. They should be recognized and quantified to avoid any wrong interpretation of the test. This is possible thanks to the measurement of displacement fields.

Thanks to this innovative methodology to measure accurately the full creep strain field at such high temperature, the next steps, namely, identification of constitutive parameters and numerical simulations, become possible to predict the lifetime of a structure made of this ceramic in its various industrial applications.

Acknowledgements

The authors would like to thank Saint-Gobain SEFPRO for providing the ZS-ISO samples and supporting this work carried out at CREE (Centre de Recherches et d’Etudes Européen) thanks to the experimental facilities of the Laboratoire d’Application Physique.

References

1. R. W. Davidge, "Mechanical behaviour of ceramics." Cambridge Solid State Science Series, (1979).

2. *W. R. Cannon and T. G. Langdon, "Creep of ceramics," J. Mat. Sci., 18[1] 1-50 (1983).*
3. *D. S. Wilkinson, "Creep Mechanisms in Multiphase Ceramic Materials," J. Am. Ceram. Soc., 81[2] 275-99 (1998).*
4. *G. D. Quinn and R. Morrell, "Design Data for Engineering Ceramics: A Review of the Flexure Test," J. Am. Ceram. Soc., 74[9] 2037-66 (1991).*
5. *L. Massard, "Etude du fluage de réfractaires électrofondus du système alumine-zircone-silice," PhD thesis, École Nationale Supérieure des Mines de Paris (2005).*
6. *G. Dusserre, F. Nazaret, L. Robert, and T. Cutard, "Applicability of image correlation techniques to characterise asymmetric refractory creep during bending tests," Journal of the European Ceramic Society, 33[2] 221-31 (2013).*
7. *P. Leplay, J. Réthoré, S. Meille, and M.-C. Baietto, "Identification of asymmetric constitutive laws at high temperature based on Digital Image Correlation," J. Europ. Ceramic Soc., 32[15] 3949-58 (2012).*
8. *F. Hild, E. Amar, and D. Marquis, "Stress Heterogeneity Effect on the Strength of Silicon Nitride," J. Am. Ceram. Soc., 75[3] 700-02 (1992).*
9. *E. Blond, N. Schmitt, F. Hild, J. Poirier, and P. Blumenfeld, "Modeling of high temperature asymmetric creep behavior of ceramics," J. Eur. Ceram. Soc., 25 1819-27 (2005).*
10. *V. Laws, "Derivation of the tensile stress-strain curve from bending data," J. Mat. Sci., 16[5] 1299-304 (1981).*
11. *M. Grédiac and F. Hild (eds.), "Full-Field Measurements and Identification in Solid Mechanics," 496 p. ISTE / Wiley, London (UK), 2013.*
12. *J. S. Lyons, J. Liu, and M. A. Sutton, "High-temperature deformation measurements using digital-image correlation," Exp. Mech., 36[1] 64-70 (1996).*
13. *J. Liu, J. Lyons, M. Sutton, and A. Reynolds, "Experimental Characterization of Crack Tip Deformation Fields in Alloy 718 at High Temperatures," J. Eng. Mat. Technol., 120[1] 71-78 (1998).*
14. *B. Pan, D. Wu, and Y. Xia, "High-temperature deformation field measurement by combining transient aerodynamic heating simulation system and reliability-guided digital image correlation," Opt. Las. Eng., 48[9] 841-48 (2010).*
15. *B. M. B. Grant, H. J. Stone, P. J. Withers, and M. Preuss, "High-temperature strain field measurement using digital image correlation," J. Strain Anal. Eng. Design, 44[4] 263-71 (2009).*
16. *B. Pan, D. Wu, Z. Wang, and Y. Xia, "High-temperature digital image correlation method for full-field deformation measurement at 1200°C," Meas. Sci. Technol., 22[1] 015701 (2011).*
17. *J. T. Hammer, J. D. Seidt, and A. Gilat, "Strain Measurement at Temperatures Up to 800°C Utilizing Digital Image Correlation," pp. 167-70. in Advancement of Optical Methods in Experimental Mechanics, Volume 3***.** *Conference Proceedings of the Society for Experimental Mechanics Series. Edited by H. Jin, C. Sciammarella, S. Yoshida, and L. Lamberti. Springer International Publishing, 2014.*
18. *M. D. Novak and F. W. Zok, "High-temperature materials testing with full-field strain measurement: Experimental design and practice," Rev. Sci. Instr., 82[115101] (2011).*
19. *M. De Strycker, L. Schueremans, W. Van Paepegem, and D. Debruyne, "Measuring the thermal expansion coefficient of tubular steel specimens with digital image correlation techniques," Opt. Las. Eng., 48[10] 978-86 (2010).*
20. *B. Pommier, F. Hild, and E. Charkaluk, "Analyse d'une éprouvette de fatigue thermomécanique par corrélation d'images," pp. 359-66 in Photomécanique 2001. Edited by Y. Berthaud, M. Cottron, J.-C. Dupré, F. Morestin, J.-J. Orteu, and V. Valle.*
21. *R. B. Berke and J. Lambros, "Ultraviolet digital image correlation (UV-DIC) for high temperature applications," Rev. Sci. Instrum., 85 045121 (2014).*
22. *B. Pan, D. Wu, and J. Gao, "High-temperature strain measurement using active imaging digital image correlation and infrared radiation heating," J. Strain Anal. (2013).*
23. *X. Guo, J. Liang, Z. Tang, B. Cao, and M. Yu, "High-temperature digital image correlation method for full-field deformation measurement captured with filters at 2600°C using spraying to form speckle patterns," OPTICE, 53[6] 063101 (2014).*

24. *M. Vautrot, P. Balland, O. S. Hopperstad, L. Tabourot, J. Raujol-Veillé, and F. Toussaint, "Experimental Technique to Characterize the Plastic Behaviour of Metallic Materials in a Wide Range of Temperatures and Strain Rates: Application to a High-Carbon Steel," Exp. Mech., 54[7] 1163-75 (2014).*
25. *F. Hild and S. Roux, "Digital Image Correlation," pp. 183-228. in Optical Methods for Solid Mechanics. A Full-Field Approach. Edited by P. Rastogi and E. Hack. Wiley-VCH, Weinheim (Germany), 2012.*
26. *J. Réthoré, F. Hild, and S. Roux, "Extended digital image correlation with crack shape optimization," Int. J. Num. Meth. Eng., 73[2] 248-72 (2008).*
27. *G. Besnard, F. Hild, and S. Roux, "``Finite-element'' displacement fields analysis from digital images: Application to Portevin-Le Châtelier bands," Exp. Mech., 46 789-803 (2006).*
28. *F. Hild, S. Roux, R. Gras, N. Guerrero, M. E. Marante, and J. Flórez-López, "Displacement Measurement Technique for Beam Kinematics," Opt. Lasers Eng., 47 495-503 (2009).*
29. *P. Leplay, J. Réthoré, S. Meille, and M.-C. Baietto, "Damage law identification of a quasi brittle ceramic from a bending test using Digital Image Correlation," Journal of the European Ceramic Society, 30[13] 2715-25 (2010).*
30. *S. P. Timoshenko, "Strength of Materials," 3rd edition ed. Krieger Publishing Company (3rd edition), (1976).*
31. *K. Triconnet, K. Derrien, F. Hild, and D. Baptiste, "Parameter choice for optimized digital image correlation," Opt. Lasers Eng., 47 728-37 (2009).*
32. *A. Delmas, Y. Le Maoult, J.-M. Buchlin, T. Sentenac, and J.-J. Orteu, "Shape distortions induced by convective effect on hot object in visible, near infrared and infrared bands," Exp. Fluids, 54[4] 1-16 (2013).*
33. *A. Bouterf, S. Roux, F. Hild, G. Vivier, X. Brajer, E. Maire, and S. Meille, "Damage law identification from full-field displacement measurement: Application to four-point bending test for plasterboard," Eur. J. Mech. A/Solids, 49 60-66 (2015).*